

Characterization of the Interfacial Toughness in a Novel “GaN-on-Diamond” Material for High-Power RF Devices

Dong Liu,^{*,†,‡,§,||,⊥,ID} Stephen Fabes,[‡] Bo-Shiuan Li,[‡] Daniel Francis,[§] Robert O. Ritchie,^{||,⊥,ID} and Martin Kuball[†]

[†]School of Physics, University of Bristol, Bristol BS8 1TL, United Kingdom

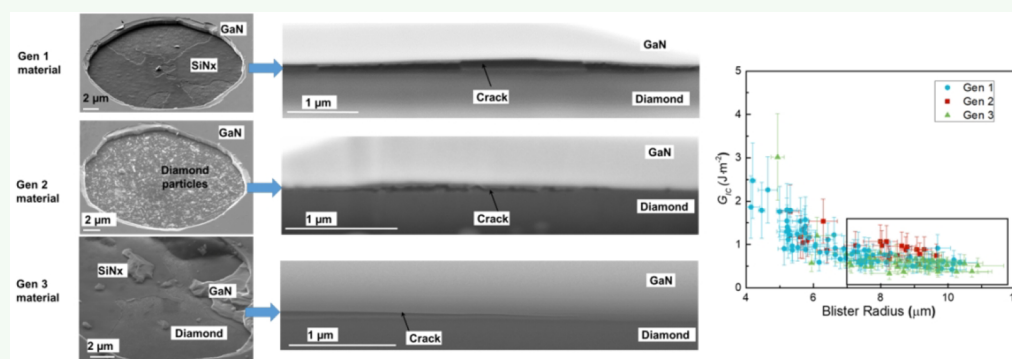
[‡]Department of Materials, University of Oxford, Oxford OX1 3PH, United Kingdom

[§]Akash Systems, San Francisco, California 94108, United States

^{||}Department of Materials Science & Engineering, University of California, Berkeley, Berkeley, California 94720, United States

[⊥]Materials Sciences Division, Lawrence Berkeley National Laboratory, Berkeley, California 94720, United States

Supporting Information



ABSTRACT: GaN thin film integrated to polycrystalline diamond substrates is a novel microwave transistor material with significantly improved heat dissipation capability. Due to the thermal and mechanical properties mismatch between GaN and diamond, a natural concern arises in terms of its interfacial stability as currently there is no established method to evaluate the interfacial toughness in GaN-on-diamond material. Using three generations of “GaN-on-Diamond” materials with varying process parameters, a comprehensive study has been carried out to identify the most appropriate fracture mechanics-based methods for reliable evaluation of the interfacial toughness in this novel material system. Several techniques were assessed, and the results are cross-compared; these include an ex situ nanoindentation induced buckling method and two-step indentation approach together with several analytical models. Additionally, a microcantilever bending method was adopted to measure an upper bound for the interfacial fracture toughness. For the three generations of materials, the interfacial toughness, G_{Ic} , was determined to be 0.7, 0.9, and 0.6 $\text{J}\cdot\text{m}^{-2}$, respectively. Postmortem analysis of the micro- and nanostructure of fractured interfaces indicated that the systems with better heat spreading capability displayed smoother fracture surfaces, i.e., were more brittle due to the lack of active toughening mechanisms. Potential modifications to the interface for improved mechanical stability were proposed based on the experimental results.

KEYWORDS: GaN-on-diamond, interfacial mechanics, fracture toughness, micromechanical testing, nanoindentation, thin film buckling

1. INTRODUCTION

“GaN-on-Diamond” is a material with great potential for ultrahigh power microwave electronics and ultimately for future high-powered monolithic microwave integrated circuits (MMIC), enabling power densities far greater than what is possible with current commercial GaN-on-SiC devices. Applications range from microwave electronics for 5G with several orders of magnitude higher bit rates compared to 4G, satellite-to-earth communication systems to radars where higher power microwave devices will allow a significant reduction of blind spots. The underlying reason for the

improved performance of GaN-on-Diamond devices is that diamond has a much higher thermal conductivity than SiC, up to 2000 W/mK for diamond vs 450 W/mK for SiC.^{1,2} For example, Pomeroy et al.³ reported a 40% decrease in peak channel temperature than in a similar GaN-on-SiC device, comparing the same-to-same device layout. For effective heat-

Received: December 4, 2018

Accepted: February 18, 2019

Published: February 18, 2019

spreading, the diamond is typically less than a micrometer away from the active device area, to maximize heat extraction.

1.1. Manufacture of GaN-on-Diamond and Its Challenges. There are many ways to produce GaN-on-Diamond materials. The most common method of attaching GaN to diamond was initially performed by Group4Labs^{4,5} (Figure 1). In this method, the AlGaIn/GaN active layers are

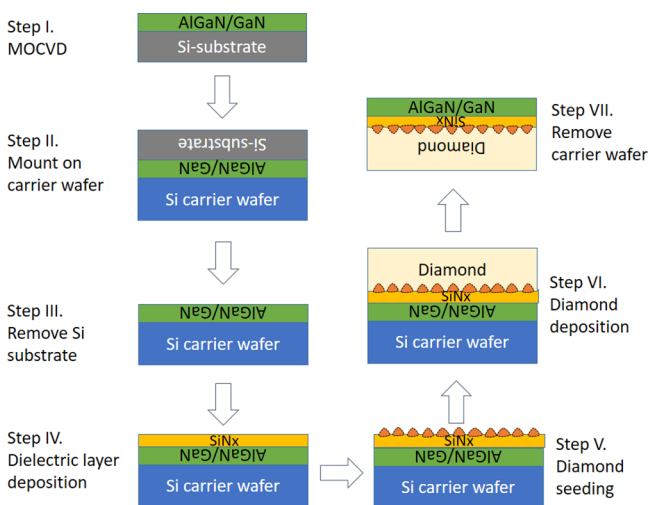


Figure 1. Schematic of the main steps for processing a GaN-on-Diamond wafer.

grown on traditional substrates such as Si before attaching the device structure to a carrier wafer (usually Si). A dielectric layer (SiN_x) is then grown onto the GaN, after removal of the original substrate, and used as a seeding bed for the subsequent diamond growth which usually utilizes micro- or nanosize diamond seeds.^{6,7} Wafers can be as large as 4–6 inches.

Alternatively, GaN devices have been directly bonded to diamond⁸ or GaN is grown epitaxially onto single crystal diamond substrates, although the latter approach tends to contain unwanted low-angle grain boundaries and cracks that can compromise device performance. Van Dremel et al.⁹ grew GaN directly onto (100) diamond; Hiramani et al.¹⁰ and Alomari et al.¹¹ attempted to grow AlGaIn/GaN devices onto (111) diamond, as the 3-fold symmetry of the diamond matches the 6-fold symmetry of (0001) GaN, but this resulted in unsatisfactory thermal properties at the GaN-Diamond interface. In all these cases, scaling to the wafer level was challenging.

Accordingly, it has been recognized that the approach of removing the original substrate and growing diamond on GaN is most promising for commercial exploitation. Both hot filament chemical vapor deposition (HF-CVD) diamond as well as microwave plasma assisted CVD (MW-CVD) have been used for GaN-on-Diamond technology though it is easier to achieve a higher thermal conductivity diamond with MW-CVD.^{1,12} As many of the early challenges, involving wafer bow, material quality control and reproducibility, have been effectively solved, the production of GaN-on-Diamond devices is on track to become commercially viable.^{7,13}

Taking full advantage of the diamond thermal properties also requires reducing gate pitch in the devices, which can enable in excess of three times greater power densities and device performance than GaN-on-SiC can provide.^{1,14} Among the many factors that impact the heat sinking capability of

GaN-on-Diamond, most pertain to the nature of the interface, in particular the thickness of the diamond nucleation layer SiN_x . For example, as the SiN_x is amorphous, it exhibits a low thermal conductivity such that it must be kept as thin as possible.¹ This, however, can be technologically challenging, as the SiN_x nucleation layer has to be made much thinner than ~ 20 nm such that any interfacial flaws will adversely affect its mechanical stability.

Under typical device operation, the temperature at the GaN/Diamond interface ramps between -65 and 200 °C, resulting in interfacial thermal strains due to mismatched thermal coefficients of expansion ($\text{GaN } \alpha_s = 5.59 \times 10^{-6} \text{ K}^{-1}$, $\alpha_c = 3.17 \times 10^{-6} \text{ K}^{-1}$; diamond $\alpha = 1.05 \times 10^{-9} \text{ K}^{-1}$). As both materials are stiff (Young's moduli are $E_{\text{dia}} = 1050$ GPa and $E_{\text{GaN}} = 295$ GPa), this gives rise to significant local stresses. Therefore, the interface toughness, which characterizes its inherent structural integrity to withstand mechanical failure, is critical to the development and reliable operation of this novel material. Despite this, there has been no comprehensive study to date aimed at identifying the most suitable mechanical characterization methods for this class of GaN-on-Diamond materials. This is the prime rationale for the present study.

1.2. Interfacial Mechanics. Many of the methods for the use of interface fracture mechanics for packaging problems were developed in the 1990s.¹⁵ All methods strive to measure a practical adhesion or toughness value rather than the thermodynamic work of adhesion as some plasticity or other energy-dissipating mechanisms always occur. It is considered that such practical toughness values better reflect the “strength” of a dissimilar, or similar material interface in service.^{15,16} Specifically, the mode I fracture toughness (G_{Ic}) is often quoted as it represents a number that is readily comparable between materials.

Most interfacial mechanics studies have focused on metal/ceramic interfaces, generally for thermal barrier coatings and semiconductor interconnects.^{17–22} There have been fewer studies performed on ceramic/ceramic interfaces, or more generally interfaces between two brittle materials, as they are often weak and not engineered to be load-bearing. Modified macroscopic test geometries, such as sandwiche bending tests, first developed by Charalambides and co-workers,^{23,24} and the Brazilian disc with a multilayer at the center,^{25,26} are popular for the study of interfacial toughness under mode I and mixed-mode conditions, in particular for semiconductor materials.^{19,27} For these types of tests, the sample preparation, either using diffusion or epoxy method to bond the sample to the substrate, has the potential to alter the original material and its fracture behavior.

Another set of techniques for characterizing the interface toughness have focused on buckling or blistering of thin films; first developed by Dannenberg,²⁸ these measure the dimensions of the buckle where G_{Ic} can be obtained.^{16,29} In these cases, indentation methods, either nano- or microscale, are employed to cause the buckling. Often the analyses of these experiments require the indent to remain within the film layers,^{30,31} which can limit the achievable plastic driving force for delamination. To resolve this problem, Kriese et al.³² used a superlayer which allowed greater indentation depths to be used; the superlayer additionally adds significant compressive stress, making delamination via indentation easier to achieve especially for metallic films on ceramics.^{22,33–36} However, superlayers often can complicate the fracture behavior; moreover, the harsh deposition conditions may cause

unwanted changes to the original interface properties and lead to multiple surface³⁷ and interfacial cracking events that are not necessarily taken into account in the analyses.^{34,38–41}

Several other methods have also been documented, such as scratch tests,³⁵ cross-sectional indentation,^{17,42} microwedge indentation^{43,44} and energy-balance techniques techniques,^{45–49} all of which have their own particular advantages and disadvantages for specific applications.

In this work, we utilize an ex situ instrumented nano-indentation induced blistering method and employ four analytical models for the interpretation of results, which are evaluated in terms of the input parameters and their limitations for this particular system of a brittle “ceramic-like” film on a stiff substrate. Additionally, a microcantilever bending based experimental configuration was developed, based on the He and Hutchinson analysis⁶⁸ of an elastic crack impinging on a dissimilar material interface, in order to provide an evaluation of an upper bound for the interfacial toughness.

2. EXPERIMENTAL PROCEDURES

2.1. Materials. Three generations of GaN-on-Diamond wafers were studied and denoted Gen 1, 2, and 3 according to the iterations of manufacture techniques. Main steps for processing such wafers are shown in Figure 1 and general growth conditions can be found in the literature.^{50,51} The thickness of GaN layer varied between 0.7 and 0.9 μm across the wafers with the diamond grown to be ~ 100 μm thick. The grain size of the diamond was found to be nanoscale near the interface and increases to ~ 20 μm at the surface of the diamond layer.⁵⁰ The thickness of the SiN_x , the average size of the diamond seeding particles, residual stresses in the GaN film, measured using Raman spectroscopy,⁵² and the thermal boundary resistance (TBR_{eff}) at the interface are shown in Table 1.

Table 1. Interface Properties of the Three Generations of GaN-on-Diamond tested (refs 1 and 53)

materials (gen no.)	SiN thickness (nm)	diamond seeding particle size (nm)	residual stress in GaN (MPa)	$\text{TBR}_{\text{eff}}/\text{m}^2 \text{ K GW}^{-1}$
1	50	~ 100	400	33
2	36	~ 50	100	22
3	41	~ 30	100	15

In particular, the SiN_x in Gen 2 was abraded with SiC grit paper before seeding whereas in Gen 3 a 5 min ultrasonic bath process was introduced to disperse the particles uniformly. All the samples had an additional protective layer of SiN_x about 10–20 nm on the GaN surface, but it was not considered to affect the indentation process. For the indentation tests, $5 \times 5 \text{ mm}^2$ wafer samples were used. They were cleaned by sonicating in acetone and then ethanol before being mounted onto aluminum JEOL specimen stubs ($E_{\text{Al}} \sim 70$ GPa) using a very thin layer of silver ElectroDag (Agar Scientific). The results were compared to samples mounted by a thin layer of crystalbond glue, and found to be completely consistent which indicated high confidence in the experimental measurements. To limit damage, a holder for these stubs, compatible with the nanoindenter, was designed to allow the samples to be transferred between instruments without demounting the samples.

2.2. Experimental Methods. Experiments involved the use of a nanoindenter to cause delamination at the GaN/Diamond interface for the quantification of the interfacial toughness. Specifically, a NanoindenterXP (Agilent technologies) was employed, with a diamond Berkovich tip (Synton-MDP), which has a three-pointed pyramid tip with a half angle of 62.57° . The tip was calibrated at the beginning of the project by making an array of nine indents to a depth of 2 μm in a block of fused silica.

During the indentation, the indenter load was altered by setting a fixed displacement, of 600–900 nm, with each displacement repeated 3–15 times; a constant strain rate of 0.5 s^{-1} was used throughout. There were two hold periods (Figure 2a): one at the maximum load to allow the system to settle, the other to measure the thermal drift, which was kept below 0.1 nm s^{-1} . The indents were formed in arrays spaced 50 to 60 μm apart to avoid elastic/plastic interactions between the blisters (Figure 2b). The maximum load and displacement were taken from the load–displacement curves and the modulus, hardness, and plastic indent depth were extracted using the Oliver and Pharr⁵³ method.

In addition, to the monotonic indentation approach described above, a two-step method was also used as described by Lu et al.⁴⁸ This involved two loading cycles with a small holding load (5% peak load for 5 s) in between (Figure 2c). The same tip, as employed for the monotonic loading, was used and the loading and unloading rate was $2000 \mu\text{N s}^{-1}$ to give a similar strain rate. In the second unloading curve, an “elbow point” appeared which indicated that the interfacial flaw was being closed. Integrating both curves up to the elbow point and the value on the unloading curve (W_1) for the first indent was subtracted from that of the second indent (W_2) to give the work of delamination (Figure 2d).

After indentation, atomic force microscopy (AFM) was used to measure the dimension of the blisters. An AFM 5400 instrument (Agilent Technologies, Oxford Materials Characterization Service) was used with aluminum-coated silicon tips (Mikromasch). The tips were 12–18 μm in height with a conical half angle of 8° (uncoated). Scanned areas were typically $\sim 30 \times 30 \mu\text{m}^2$; 512 points per line at 0.5 lines/s was used across all indents to maximize accuracy. Some of the indents were also measured using an Olympus BX60 M optical microscope, with no polarization and a 100 \times lens, to compare with AFM. Finally, a Zeiss Auriga Focused Ion Beam (FIB) instrument was used to section and examine the Gen 1 material blisters that had been measured with the optical and AFM. Here, 30 kV and a FIB current of 1 nA were used.

For the microcantilever bending, specimens were made using FEI FIB200 and Zeiss Auriga instruments (David Cockayne Centre for Electron Microscopy, Oxford University), on a Gen 1 wafer. The steps for the two methods (M1 and M2) for cutting the cantilevers are shown in Figure 3a. For the larger cuts, a FIB current of 4 or 5 nA was used, with 1 nA for cleaning. To form the notches, 10 pA FIB current was used for 6 s to ensure that as sharp a notch as possible was created.

Lastly, transmission electron microscopy (TEM) images were undertaken on Dualbeam Helios FIB milled samples using a FEI Tecnai OSIRIS STEM (150 kV) in each material and the interfacial attachment between GaN, SiN_x and diamond were examined to assist the understanding of the fracture mode at the interface.

The cantilevers were tested using a Nanoindenter-G200 (Agilent Technologies). A Berkovich tip was used to first scan the cantilever, in AFM mode, with 24 x -points and 250 y -points to precisely locate the loading point. A scanning load of 2 μN was used to avoid damaging the cantilevers. During testing the flat edge of the tip was aligned toward the cantilever to ensure bending occurred rather than indentation (Figure 3b). Cantilevers were loaded slowly during the test, at $4 \mu\text{N s}^{-1}$, to encourage interfacial failure. After testing the cantilever fracture surfaces were observed in a Zeiss Auriga microscope.

3. RESULTS

3.1. Characterization of the Buckling Geometry. First of all, the Young’s modulus E and hardness H of the GaN film in all three generations of the GaN-on-Diamond materials were measured; values of $E_{\text{GaN}} = 295 \pm 10$ GPa and $H_{\text{GaN}} = 19.1 \pm 1$ GPa were obtained, similar to those in the literature ($E_{\text{GaN}} = 287\text{--}320$ GPa, $H_{\text{GaN}} = 12\text{--}22$ GPa).^{54,55} As the subsequent analysis is based primarily on the delamination size and the buckle geometry, a reliable method to characterize these

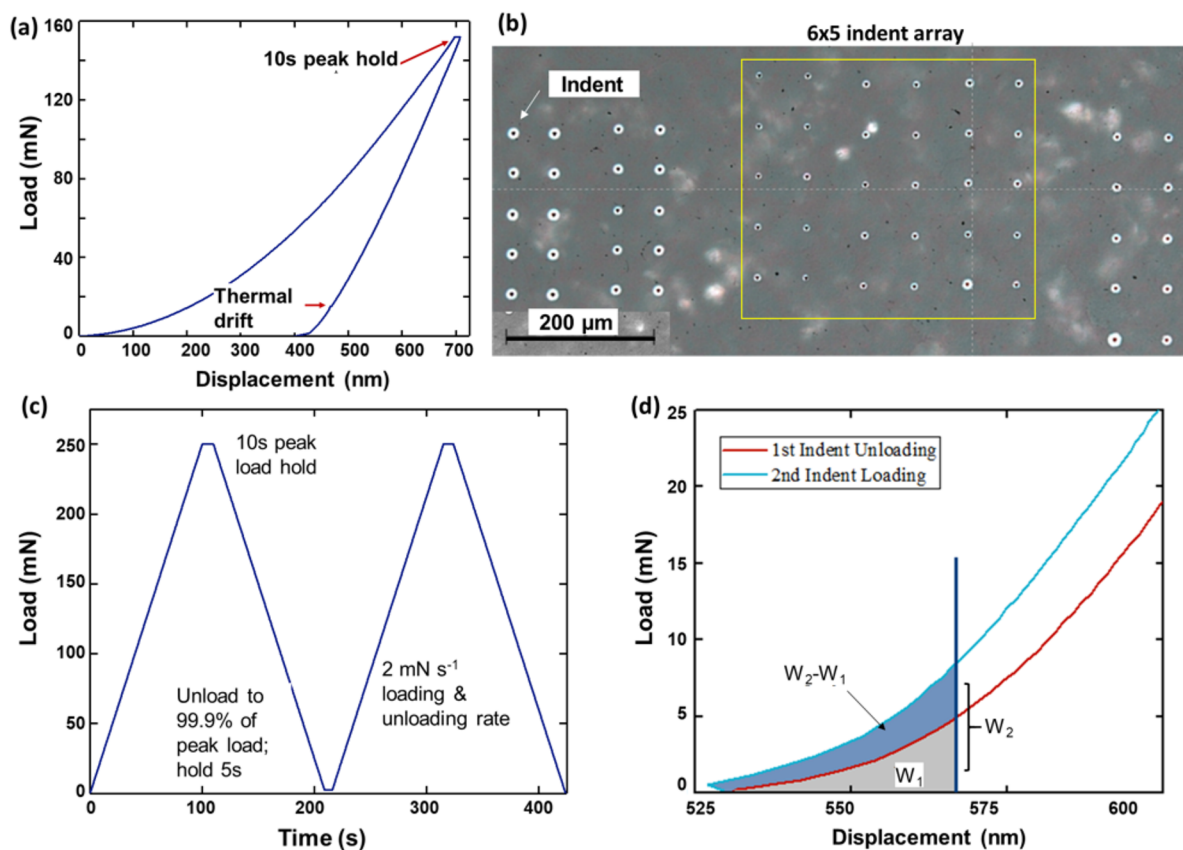


Figure 2. (a) Typical indentation load–displacement curve, showing the two hold periods; (b) arrays of indentation-induced blisters on a Gen I wafer; (c) typical load–time curve, and (d) segmentation of the work of delamination for the two-step method.

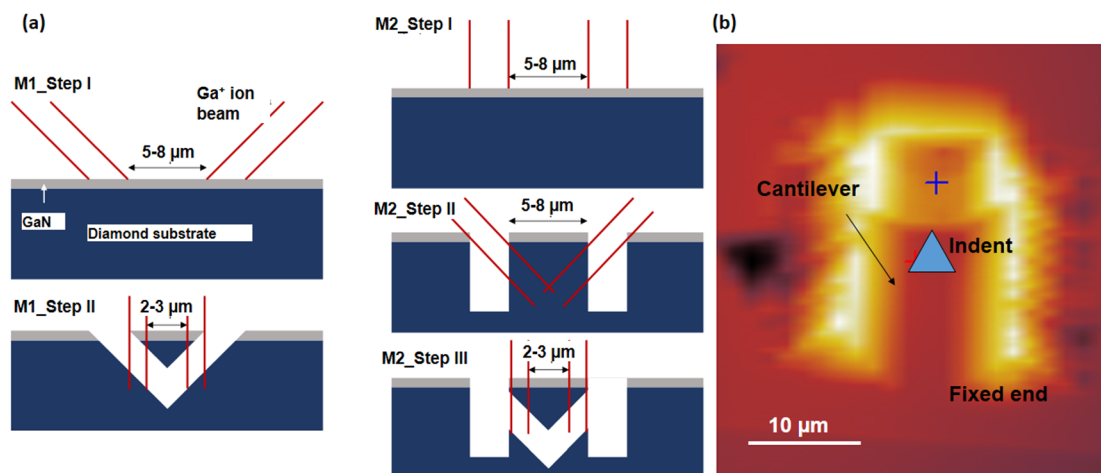


Figure 3. (a) FIB methods used to make pentagonal cantilever cross sections. Further polishing steps and notching were carried out after stages shown in (a). (b) Scanned cantilever, loading position (marked by the blue cross), and testing parameters. Triangle shows tip orientation in testing.

parameters had to be established. As the buckling heights for GaN-on-Diamond are much lower than those of other materials systems such as metal on stiff substrate, it is not possible to directly translate experience from the latter material systems.

As such, three approaches, AFM, optical imaging, and FIB cross-sectioning, were used with the results compared. Specifically, for AFM and optical methods, three-line profiles were taken across the indent with a fourth taken away from the indent to calculate the average height of the sample in the

AFM data, or average gray level in the optical measurements (Figure 4a). The standard deviation in this average was derived, and a threshold was set at the average and four (AFM) or six (optical) times the standard deviation. The maximum height of the buckle was then subtracted from the threshold to derive the actual buckle height. The threshold widths were defined where the profile became flat and corrected by adding a slight random error. Other methods, such as using gradient and edge detection were tried; however, the edges of the buckle were not sharp such that these methods did not give

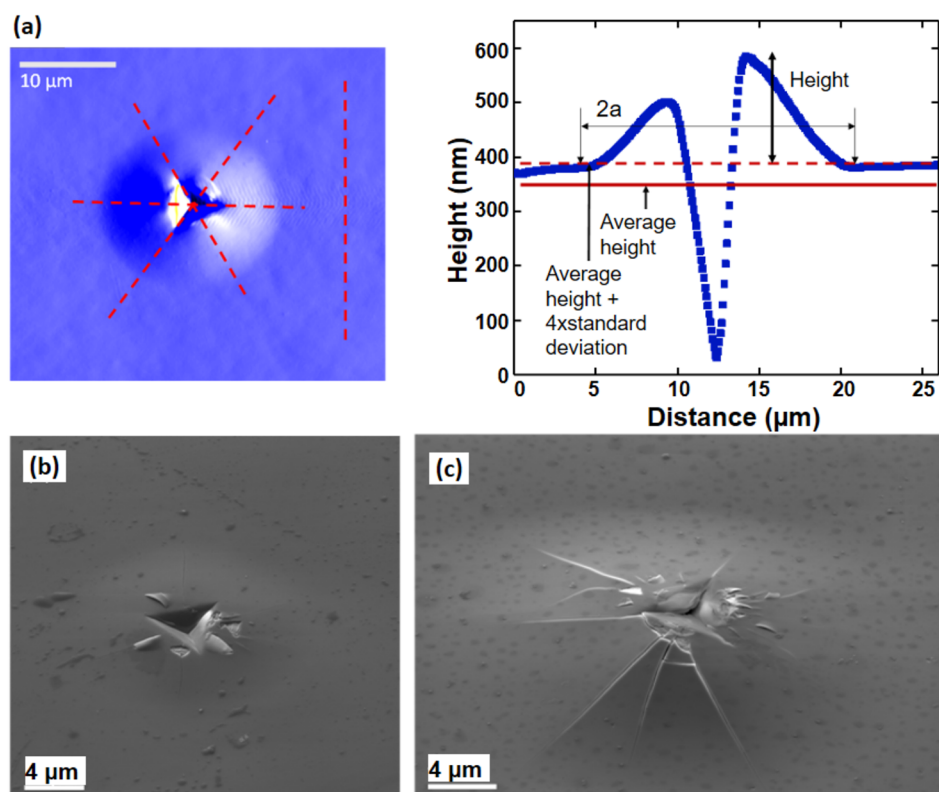


Figure 4. Process for segmenting the buckle width and height in AFM. (a) AFM image and height profile as a function of distance across the blister; (b) “qualified” blister/buckle with the protective layer chipping, and (c) “invalid” blister with large scale cracking.

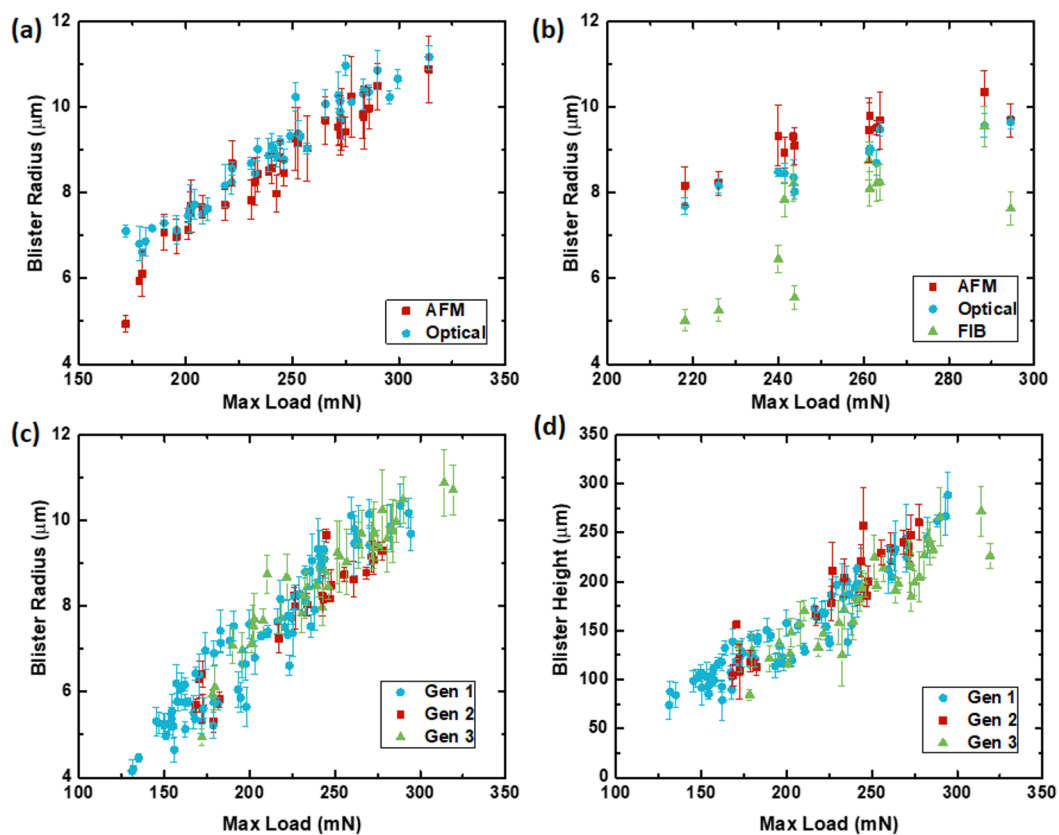


Figure 5. Comparison of the blister radius measured (a) by AFM and optical and (b) by AFM, optical with FIB sectioning. (c) Blister radius and (d) blister height plotted as a function of maximum load (mN).

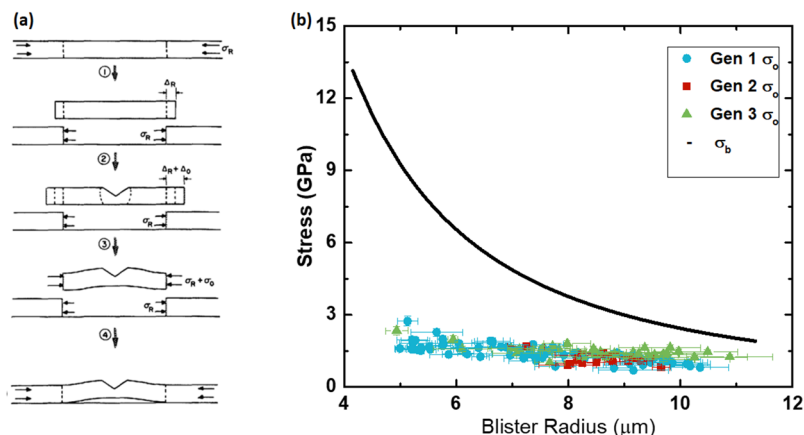


Figure 6. (a) ME analysis steps (Reproduced with permission from ref 31. Copyright 2019 AIP Publishing). (1)–(3) show dilatations from residual and indentation stress, and (4) shows the resulting edge compression. (b) Calculated indentation edge stresses and critical buckling stress.

reliable results. The AFM data were first planarized, with rows aligned with a median of differences technique, to remove artifacts using Gwyddion software.⁵⁶ It worth noting that the top thin protective layer tended to chip (Figure 4b); however, when large-scale cracking occurs, the blister/buckle was considered to be “invalid” (Figure 4c) and no further measurements were taken.

To directly compare the results of AFM and optical measurements, 95 indents were examined; the results from one of samples is presented in Figure 5a. It was found that the two methods showed good agreement in both the average and uncertainties. However, the FIB results showed a random disagreement with AFM and optical measurements. It was considered that FIB cross-sectioning tends to relax the residual stresses in the buckled layer which leads to closure of the cracks. Considering that optical method could not measure the height of the blisters, we concluded that AFM was the best method for a reliable characterization of the blister geometry. The size of all valid blisters measured in this work from all three generation of materials are presented in Figures 5c and 5d where, in addition to a linear relation existing between their height and width, both dimensions displayed a nearly linear relationship with applied load, which is typical for indentation-induced interfacial cracking.^{57–59}

3.2. Interfacial Fracture Toughness (Monotonic Loading). There are three main analytical models in the literature for analyzing such buckled blisters, namely, the Evans and Hutchinson⁶⁰ (EH) analysis, Marshall and Evans³¹ (ME), analysis and Hutchinson and Suo⁶¹ (HS) analysis. All the models consider the blister as a clamped plate undergoing Eulerian buckling. The critical, biaxial, buckling stress, σ_B , is given by⁶¹

$$\sigma_B = \frac{\mu^2 h^2 E}{12a^2(1 - \nu^2)} \quad (1)$$

where h is film height, a is blister radius, and E and ν are, respectively, the Young’s modulus and Poisson’s ratio of the film. The constant μ^2 refers to the buckling format. For a single buckle, $\mu^2 = 14.68$; for a double or annular buckle, $\mu^2 = 42.67$. The implications of this are discussed below in the Discussion section.

The EH and ME analysis focus on the indentation-induced compression (Figure 6a). The plastic indent volume, V_p , is used to calculate an expansion of the plate, assuming the

thickness of the plate is retained and that the indent volume all becomes a radial expansion.^{31,60} This expansion, Δ_0 , is given by^{31,60}

$$\Delta_0 = \frac{V_p}{2\pi ah} \quad (2)$$

V_p is calculated using the residual plastic indent depth, d_p .¹⁶ If the indenter tip is assumed to be a perfect triangular pyramid with a Berkovich area function of $24.5d^2$, then:

$$V_p = \frac{24.5}{3} d_p^3 \quad (3)$$

The indentation-induced, biaxial, compressive, edge stress is then calculated as^{31,60}

$$\sigma_0 = \frac{EV_p}{[2\pi(1 - \nu)ha^2]} \quad (4)$$

Unlike the EH analysis, the ME analysis includes a consideration of residual stresses.³¹ In both methods, $\sigma_0 > \sigma_B$ must be satisfied for buckling to occur. However, this is never achieved in any of the generations of GaN-on-Diamond samples (Figure 6b), although it is clear that buckling occurred. Therefore, the ME method is clearly not ideal for our bimaterial system, possibly because (i) GaN is a brittle anisotropic intermetallic with a Wurtzite crystal structure which could lead to errors in calculating its expansion;⁶² (ii) the ME analysis requires a stiff substrate that can fail due to plastically deforming interlayers;¹⁵ however, the SiN_x layer is thin and unlikely to have failed in this manner; (iii) the analyses are derived for thick metallic films and only consider plasticity-induced edge stresses.^{31,60} With a thin film of a brittle material, the deformation is largely elastic. Waters and Volinsky³⁶ reported ME and HS analyses were ideal for a metal films, suggesting that due to the highly brittle nature of the GaN, the ME and HE analyses are not ideal.

Hutchinson and Suo (HS)⁶¹ tackled the problem in reverse. In their analysis, the final buckle is considered and the driving stress, σ_D , to form such a buckle is then back-calculated. This avoids the assumptions concerning σ_0 and means that a residual stress in the film is not required. σ_D is calculated by rearranging the Euler buckling amplitude, B , using the measured buckle height, δ ,⁶¹ namely,

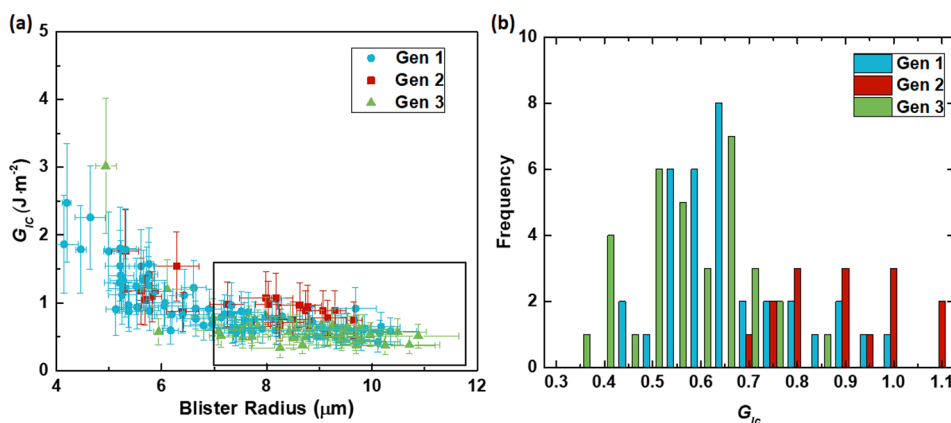


Figure 7. (a) G_{Ic} values derived from the Hutchinson and Suo (HS) method: the circled region is the valid toughness values used for the plot in (b). (b) Population histograms of the values used for calculating the average fracture toughness.

$$B = \frac{\delta}{h} = \left[\frac{1}{C_1} \left(\frac{\sigma_D}{\sigma_B} - 1 \right) \right]^{0.5} \quad (5)$$

where, $C_1 = 0.2478(1 + \nu) + 0.2231(1 - \nu^2)$. Rearranging gives

$$\sigma_D = \sigma_B \left(1 + C_1 \left(\frac{\delta}{h} \right)^2 \right) \quad (6)$$

The mixed-mode interfacial fracture toughness is then calculated using⁶¹

$$G_{Ic}(\psi) = C_2 \left[1 - \left(\frac{\sigma_B}{\sigma_D} \right)^2 \right] \frac{(1 - \nu)h\sigma_D^2}{E} \quad (7)$$

where $C_2 = [1 + 0.9021(1 - \nu)]^{-1}$.

HS then used an asymptotic solution for the phase angle (an evaluation of the mode mixity at the interface between mode I and mode II in this case), ψ , of a circular blister (the detailed description of phase angle is included in Appendix I in the Supporting Information):⁶¹

$$\psi = \tan^{-1} \left[\frac{\cos \omega + 0.2486(1 + \nu) \frac{\delta}{h} \sin \omega}{-\sin \omega + 0.2486(1 + \nu) \frac{\delta}{h} \cos \omega} \right] \quad (8)$$

where $\omega = 52.1^\circ$.⁶¹ The mode I fracture toughness, G_{Ic} , can then be determined to be⁶¹

$$G_{Ic} = \frac{G_{Ic}(\psi)}{[1 + \tan^2((1 - \lambda)\psi)]} \quad (9)$$

where, $\lambda = 0.3$ describes the shear contribution to the fracture toughness, assuming a brittle interface.⁶¹ This assumption is justifiable as all the spallation surfaces in the present GaN-on-Diamond samples show brittle interfacial fracture.

It is emphasized that although mixed-mode toughness is most relevant to bimaterial interfaces as even if one loads the interface in mode I, the modulus mismatch across the interface will still induce a mode II component, the current work extracted mode I fracture toughness (excluding the shear component at the interface) from the mixed-mode toughness based on the phase angle and compared across materials in this work. However, we accept that the mixed-mode G_{Ic} is likely a “truer” reflection of the interfacial toughness.

Recall that, in Figure 5c and d, the blister radius (a) and height (δ) were shown to have a near linear relationship with the applied load. Expanding the HS analysis yields $\delta \propto a^{4/3}$, and the index values of 1.28, 1.57, and 1.32, respectively, were obtained from the experimental results for the Gen 1, 2, and 3 GaN-on-Diamond materials. As these index numbers are near 4/3, it suggests the HS prediction aligns better with the experimental results. The calculated interfacial fracture energy is plotted in Figure 7a. There is a clear trend toward higher G_{Ic} values for smaller blisters, due to the overlapping of the plastic zones around the indenter and emanating cracks, which causes inflated G_{Ic} values as the elastic assumptions in the model are no longer met.^{32,63} Accordingly, only long crack (in this case, blister radius is about 10 times of the GaN film thickness) plateau regions were considered to reflect the fracture toughness of the interface (Figure 7b). As the average values appear close to one another, an ANOVA statistical analysis was performed (Table 2). The two ANOVA test statistics are F and

Table 2. ANOVA Analysis of the Three Populations^a

source of variation	SS	DF	MS	F	P -value	F_{crit}
between groups	1.08	2	0.54	27.96	6.19×10^{-10}	3.11
within groups	1.54	80	0.02			
total	2.62	82				

^aDF is the degrees of freedom, SS is the variance, and MS = SS/DF.

the P -value; as F is much larger than F_{crit} and P is much smaller than the hypothesis value (α) of 0.05, the analysis shows that the three populations and their averages are different. The averaged fracture toughness values for the three materials are listed in Table 3. Note that the “unpinned” data used $\mu^2 = 14.68$ for single buckle in eq 1 while $\mu^2 = 42.67$ for “pinned” double buckle results. In the GaN-on-Diamond

Table 3. Average G_{Ic} Fracture Toughness (in $J \cdot m^{-2}$) of the Interface and Associated Errors

	generation numbers of GaN-on-Diamond		
	1	2	3
no. of indents	35	15	33
unpinned	0.66 ± 0.2	0.87 ± 0.1	0.55 ± 0.1
pinned	5.57 ± 1.5	7.36 ± 1.1	4.63 ± 1

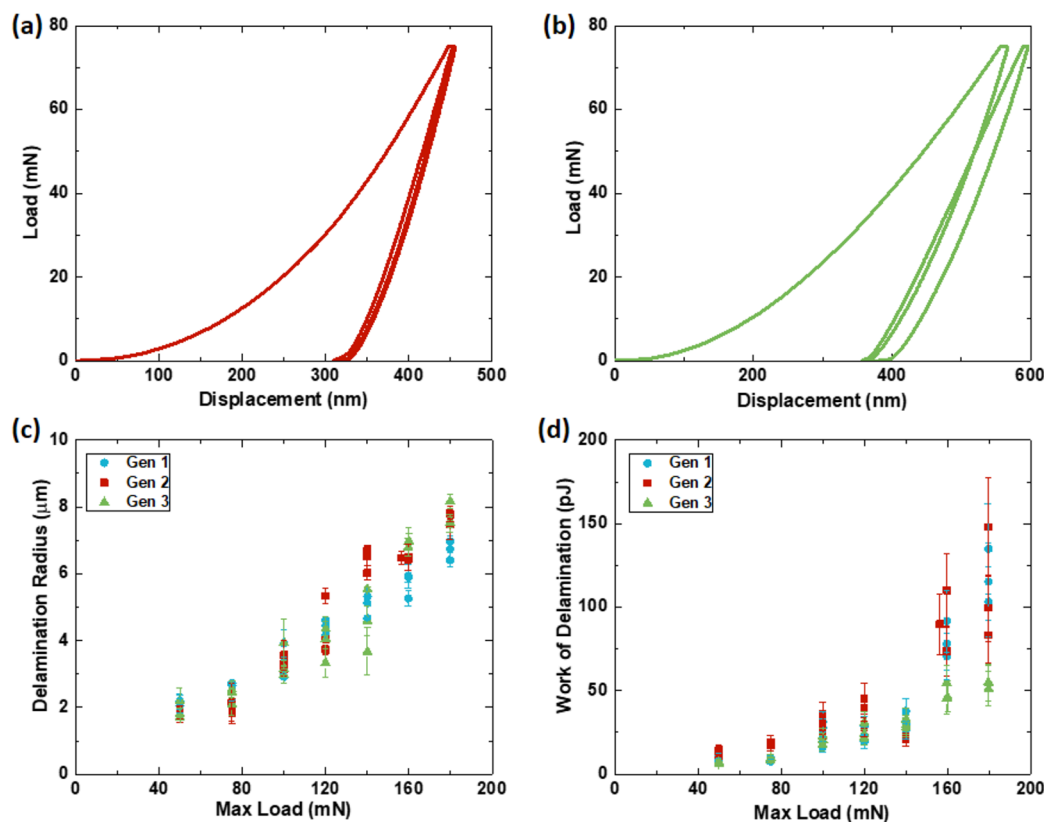


Figure 8. Typical load-unload-displacement curves for (a) Gen 2 GaN-on-Diamond samples and (b) corresponding Gen 1 and Gen 3 materials. (c) Delamination radii and (d) work of delamination as a function of maximum load for the two-step method.

system, it is considered the buckles are unpinned, i.e., a single buckle, and this is validated by the two-step method and the microcantilever testing. This is discussed further in the Discussion section.

3.3. Interfacial Fracture Toughness (Two-Step Method). Two-step method for the measurement of interfacial toughness was first proposed by Xie and Huang⁴⁶ and builds on the analysis of Hainsworth et al.⁴⁵ by conducting two consecutive indentation loading cycles on one site. However, as some clarity on the method was lacking in published literature, the present work sought to clarify the model's theoretical basis for the use on the GaN-on-Diamond materials, specifically by comparing the results with those derived from the monotonic methods.

In this thermodynamic model, there are three main energies of interest: W is the external work done by the indenter, U_c is the energy related to the crack, and U_E is the elastic strain energy stored in the film.⁴⁵ The external work done by the indenter is given by the area under the load-displacement curve.⁴⁵ Considering the two areas (1 and 2) in Figure 2d, during the unloading of the first indent, the indenter work is balanced by the elastic strain energy stored in the film and the energy release of the crack. U_c is negative as energy is being released as the crack grows, such that

$$W_1 = U_{E1} - U_c \quad (10)$$

On reloading, the indenter flexes the film and the indenter work is matched by the elastic strain energy in the deflected film:

$$W_2 = U_{E2} \quad (11)$$

The elastic strain energy in the fully flexed film is then assumed to be equal to the elastic strain energy in the film during the first unloading. This is reasonable as the dimensions of the delaminated film section can be assumed to be equal. To identify the point where the film is fully flexed, the elbow point is found (Figure 2d),^{46,48} which represents the point where the indenter has closed the interfacial flaw and is pushing on both the film and substrate, rather than the suspended film.⁴⁸

Taking $W_2 - W_1$ and using $U_{E1} \approx U_{E2}$:

$$W_2 - W_1 = U_{E2} - U_{E1} + U_c \approx U_c \quad (12)$$

where U_c is given by

$$U_c = G_{ic}(\psi)\pi r^2 \quad (13)$$

where $G_{ic}(\psi)$ is the mixed-mode fracture toughness of the interface and r is the delamination radius. Inserting this into $W_2 - W_1$ and rearranging gives

$$G_{ic}(\psi) = \frac{W_2 - W_1}{\pi r^2} \quad (14)$$

The model implicitly assumes the majority of crack growth occurs at the end of unloading, due to tensile stresses at the interface. The original authors^{46,48} claimed that these were plasticity-derived, but for GaN-on-Diamond they are likely to be predominantly elastic. In this study, final delamination radii were used for r and no crack growth was assumed to occur during the second loading cycle.

Based on the above understanding, example load-displacement graphs for 75 mN indents are shown in Figure 8. For the Gen 2 material, the deformation associated with the second

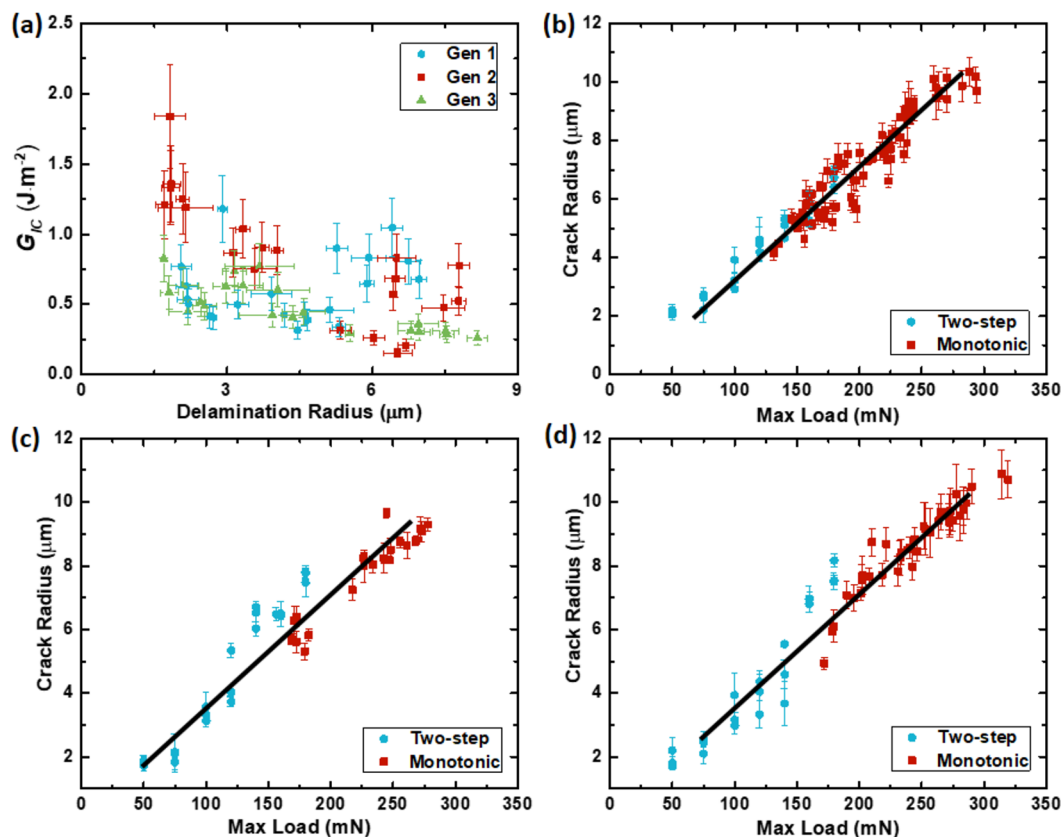


Figure 9. (a) Mode I toughness G_{Ic} at the interface estimated using the two-step indentation method. Comparison of the crack radii as a function of the maximum indenter load based on the two-step and monotonic loading methods for the (b) Gen 1, (c) Gen 2, and (d) Gen 3 GaN-on-Diamond materials.

indent was essentially elastic (Figure 8a), while for the Gen 1 and Gen 3 materials, the second loading curve showed some extension and bowing (Figure 8b) suggestive of further plasticity or crack extension. In general, the Gen 3 indents were deeper due to their thicker GaN layers. The delamination radii from these tests are plotted as a function of the maximum load in Figure 8c; note that smaller indents were used in two-step method to avoid buckling. There is a plateau at the smallest crack lengths ($<2 \mu\text{m}$), which could be an indication of a threshold crack length related to the indenter geometry. The work of delamination across the three generations of GaN-on-Diamond material were calculated and plotted as a function of the maximum applied load in Figure 8d. There is a noticeable dip at 140 mN, which we believe occur at the onset of buckling or cracking of the protective film.

To derive a mode I toughness ($\psi = 0$) that is comparable with other methods from the mixed-mode fracture toughness G_{Ic} (eq 13), a phase angle of the mixed mode is needed; but this was not discussed by the original authors of the two-step method.^{46,48} However, as the system is very similar to lateral cracking in ceramics,^{58,59} a method proposed by Chen et al.⁵⁹ was used here to estimate the phase angle based on the lateral crack vs. the plastic-zone radius (R_p).

As such, R_p was derived based on its relationship with the maximum indentation depth, d_m , in the first loading cycle by the following relationship:

$$\frac{R_p}{d_m} = -12.907 \frac{H}{E} + 4.5451 \quad (15)$$

The mode I fracture toughness, G_{Ic} , is plotted in Figure 9a with the average data shown in Table 4. ANOVA analysis was

Table 4. Summary of the Two-Step Fracture Toughness Calculations

materials (gen no.)	$G_{Ic}(\psi)$ ($\text{J}\cdot\text{m}^{-2}$)	$G_{Ic}(\psi)$ error ($\text{J}\cdot\text{m}^{-2}$)	c/R_p avg	d/R_p avg	phase angle (deg)	G_{Ic} ($\text{J}\cdot\text{m}^{-2}$)	G_{Ic} error ($\text{J}\cdot\text{m}^{-2}$)
1	0.61	0.1	1.87	0.45	20	0.57	0.2
2	0.96	0.2	1.82	0.44	18	0.91	0.3
3	0.56	0.1	1.30	0.34	20	0.53	0.2

performed which suggested that the average values of the three generations of material were different, as deduced in the monotonic method (Table 5). One uncertainty in the analysis

Table 5. ANOVA Analysis of Two-Step Analysis Results

source of variation	SS	DF	MS	F	P-value	F_{crit}
between groups	1.385	2	0.693	7.681	0.0013	3.195
within groups	4.238	47	0.09			
total	5.623	49				

of the two-step method came from the circular assumption of the delamination, especially for smaller ones, where the shape of the delaminated area is more asymmetric. This error was assumed to be encompassed in the measurement error of the delamination radii. There was a random error in identifying where the flaw is fully closed, as it is probably past the

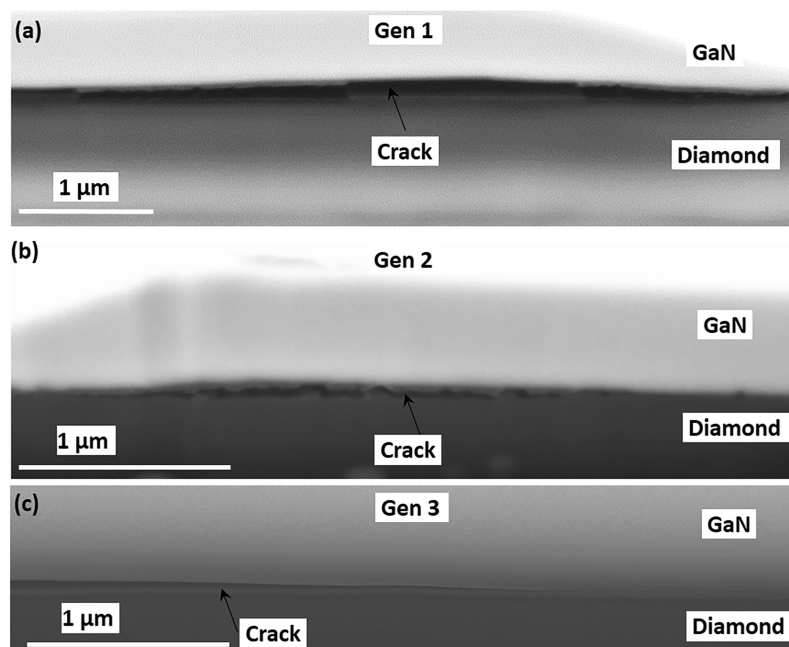


Figure 10. Cross-sectional images showing the typical fracture pattern in (a) Gen 1, (b) Gen 2, and (c) Gen 3 materials. Note the fracture patterns in (a) and (c) are both present in Gen 3 material.

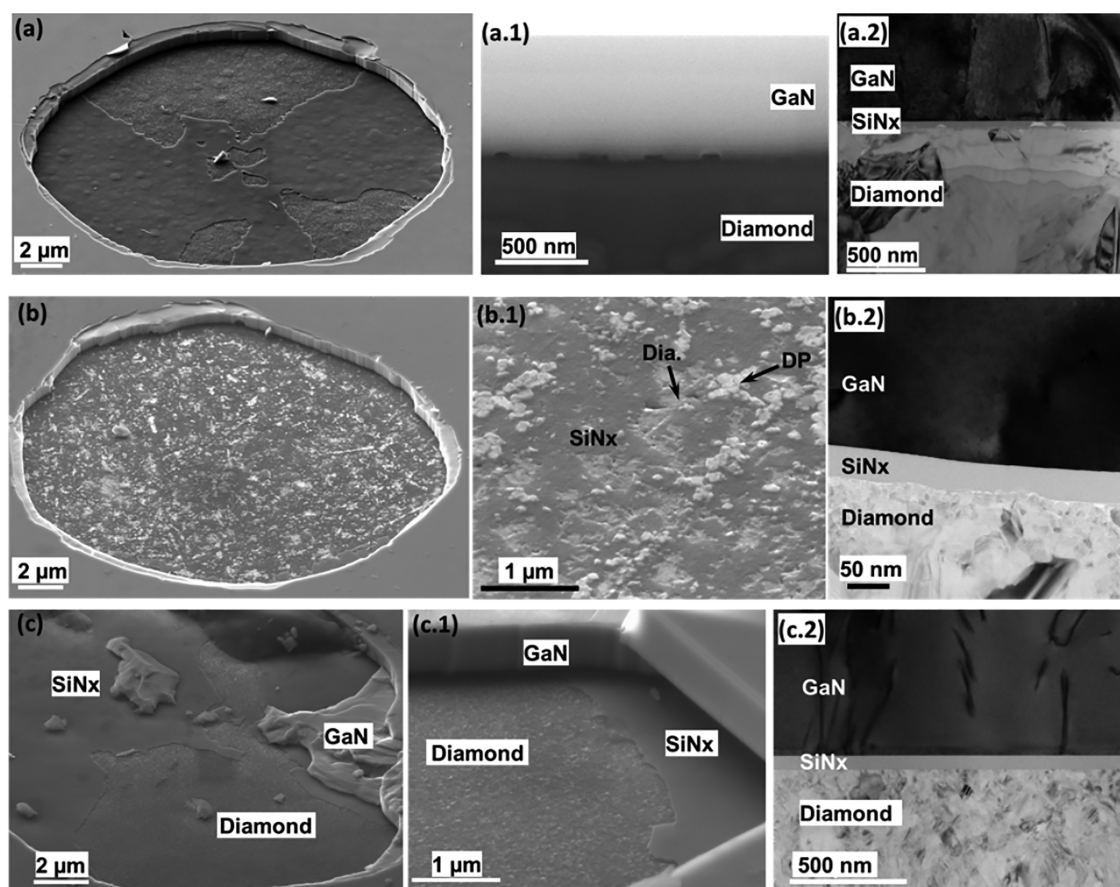


Figure 11. Spalled surface for (a) Gen 1, (b) Gen 2, and (c) Gen 3 materials. (a.1) Pinholes and (a.2) TEM cross-sectional image of Gen 1 material; (b.1) higher magnification image of (b) showing a mixture of diamond substrate (Dia.), SiNx, and diamond particles (DP) and (b.2) TEM cross-sectional image of Gen 2 material; (c.1) enlargement of (c) and (c.2) TEM cross-sectional image of Gen 3 material.

observed elbow point. Sensitivity analyses showed moving the elbow point within reasonable bounds gave $\sim 10\%$ error in

$G_{ic}(\psi)$. Average values of c/R_p and h/R_p were used to encompass the error in the approximate calculation of the

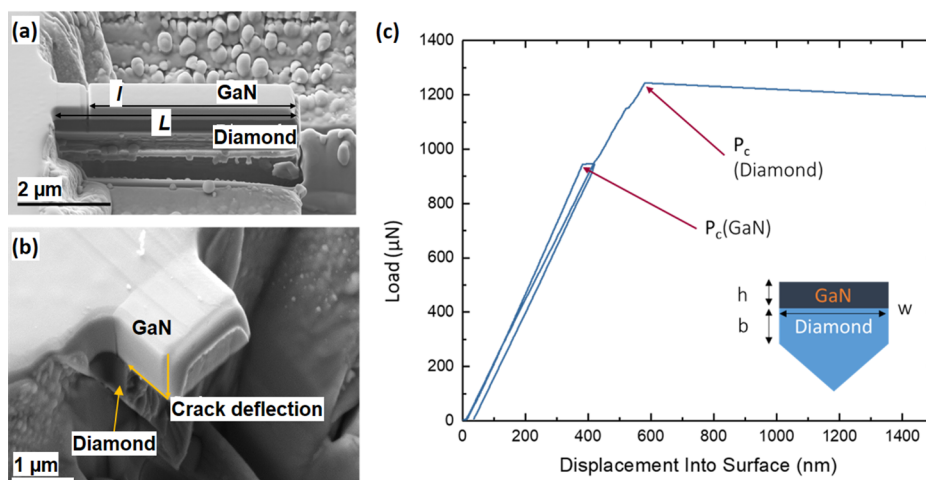


Figure 12. (a) Notched cantilever and (b) fractured cantilever after loading cycles shown in (c).

phase angle and plastic zone radius (Table 4). Based on these analysis, the results from the two-step method were found to be consistent with the HS model using an “unpinned” single buckle assumption.

The final crack population radii obtained from the two-step model were compared with that measured from the monotonic test (Figure 9b–d). Data points for all the three generations of material lie on the same linear trend, except for the Gen 2 and Gen 3 materials that had a small increase in the crack radius as the two group of data joins. This suggests that only minimal crack growth had occurred in the second loading cycle for the Gen 1 material with potentially only a small increase in crack length in the Gen 2 and 3 samples. None of this, however, had much effect on the calculated fracture toughness results (compare Tables 3 and 4).

3.4. Interfacial Failure Mode. It is common practice to section blisters to observe their failure behavior.^{35,63} However, FIB slices alone were hard to interpret due to the limited field of view. In this work, spalled indents were used to give complementary information and compare the fracture behavior between the three generations of GaN-on-Diamond material. As spallation tended to occur after blistering/buckling, it was assumed that the spalled fracture surfaces were representative of the blister fracture at the interface. The three generations of materials showed different fracture behaviors. These were analyzed qualitatively to ascertain which fracture and consequent toughening mechanisms were active.

First, both Gen 1 and 3 materials have similar toughness (Table 3 and 4) and fracture modes (Figures 10a, c) where the crack propagated along both the GaN/SiN_x and SiN_x/Diamond interface by hopping between them. Gen 1 materials presented a roughly similar fraction of failure along both interfaces (Figure 10a), whereas in the Gen 3 material, failure was more dominated by fracture on one interface (Figure 10a, c). To form these fracture surfaces, the interfacial crack must deflect through the SiN_x layer; indeed, it is evident in Figure 11a.1 that there were interfacial microflaws in Gen 1 wafers to facilitate such deflection. The TEM images of the Gen 1 material (Figures 11a.2) show clearly the mechanism behind this fracture mode; specifically, the diamond seeding-particles are less densely packed, which allows the diamond growth environment to partially etch away the SiN_x leading to the formation of microflaws. The uniformly dispersed, smaller seeding-particles of the Gen 3 material (Figure 11c, c.1)

mitigate such flaws from occurring as much less dense distributed flaws were seen. This resulted in a smoother crack path (Figure 10c) than Gen 1 although small amount of zigzag cracks were present (Figure 10a). For Gen 1, the presence of interfacial flaws (Figure 11a.1) facilitate the crack deflection and explained the evenly mixed fracture pattern in the Gen 1 material (Figure 10a). On the other hand, as the cracks are deflected at the interface, this extrinsic mechanism leads to a slightly higher toughness in the Gen 1 wafer compared to the Gen 3 material. The precise mechanisms here are by the flaws locally blunting their crack tips and/or from the crack deflection leading to crack bridging. Indeed, near the indents (Figure 10a), the crack deflections look similar to the crack bridges shown by Swanson et al.⁶⁴ As the bridges are small and widely spaced, the effect is not large.

The Gen 2 material is the toughest of the three materials; it displays a different fracture pattern in that there is a complex crack path undulating between GaN/SiN_x and SiN_x/diamond seeding layer (Figures 10b and 11b, b.1, b.2). The diamond seeding surface displays a chaotic structure with considerable roughness that would require a higher energy to propagate a crack through the seeding clusters (Figure 11b.1). Indeed, Miyazato et al.⁶⁵ provided evidence where a complex crack path could significantly raise the fracture toughness at an YBCO/Ag interface ($G_{Ic} = 80\text{--}120 \text{ J}\cdot\text{m}^{-2}$). In addition, as the cracks must deflect around the clusters of diamond particles, this could lead to crack bridging which could account for the increased toughness of the Gen 2 materials. No secondary fracture around the bridges is seen, as in large-grained ceramics, which limits the effectiveness of the bridging. The origin of the clusters in Gen 2 could be attributed to the scratching of the SiN_x before seeding, which causes the diamond particles to align with the direction of the scratches.

3.5. In Situ Microcantilever Bending. Microcantilevers with the GaN/diamond interface parallel to the beam axis were made by focus ion beam machining in Gen 1 material (Figure 12a). All samples had a pentagonal cross-section to sustain a constant width of the beam near the interface to promote the possibility of interfacial failure over cleavage fracture through the diamond. A notch, of depth $\sim 200 \text{ nm}$, was introduced into the GaN layer close to the fixed end of the cantilever and the actual depth of the notch was measured on fractured cantilever cross-section (Figure 12b). Two loading cycles were applied: the first cycle was to fracture the notch in the GaN which was

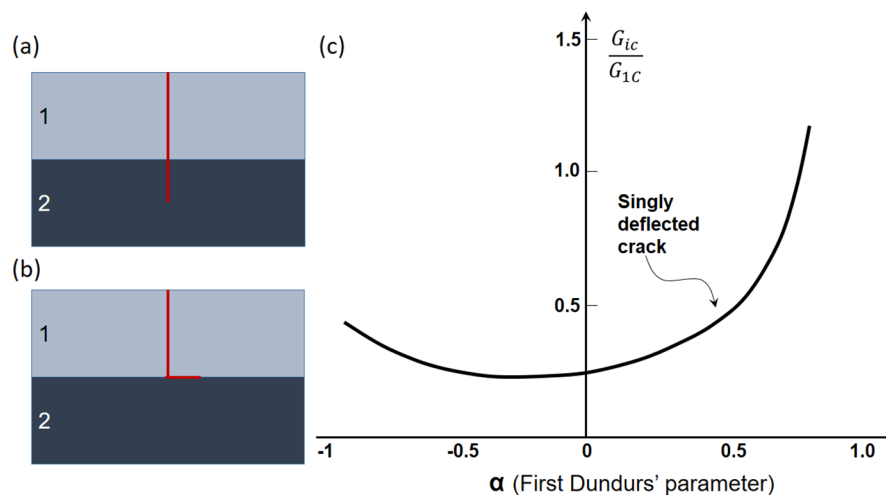


Figure 13. Crack running from material 1 (GaN) and impinging on the interface with material 2 (diamond) can either (a) penetrate or (b) arrest or deflect. (c) Diagram illustrating He and Hutchinson's linear-elastic analytical solution where whether a crack impinging on a dissimilar material interface penetrates or arrests is a function of the modulus mismatch across the interface, defined by the first Dundurs' parameter α , the interfacial (energetic) toughness G_{ic} and the (energetic) toughness of material 2 (diamond) G_{1c} .

marked by a change of the load–displacement curve, and the second loading cycle was to load the cantilever to final failure (Figure 12b, c). From the first cycle, the fracture toughness of the GaN could be derived and from the second loading cycle, by assuming an initial flaw equivalent to the diamond seeds size, the fracture toughness of the polycrystalline diamond substrate can be estimated. Based on these parameters and the final fracture mode (Figure 12b), the upper bound of the interfacial fracture toughness can be determined from the He and Hutchinson method.⁶⁸

For the measurement of the GaN toughness, the analytical solution proposed by Di Maio and Roberts⁶⁶ on notched pentagonal cantilevers was used:

$$K_{Ic} = \sigma_c \sqrt{\pi a} F\left(\frac{a}{b}\right) \quad (16)$$

where K_{Ic} is the mode I (stress-intensity based) fracture toughness and a is the crack length of interest. The fracture stress, σ_c is calculated from the failure load, P_c (Figure 12c), using beam theory. The equations must be adapted for a composite beam of two components (rectangular GaN section, and pentagonal diamond cross-section). An approximate solution was utilized:

$$\sigma_c = \frac{P_c L (\bar{y} - a)}{I_T} \quad (17)$$

where L is the test length, I_T is the total moment of inertia of the beam, and $(\bar{y} - a)$ gives the distance from the crack tip to the neutral plane. The detailed calculation of these parameters is in Appendix II in the Supporting Information. $F(a/b)$ is a geometric factor which can be approximated as the Di Maio and Roberts⁶⁶ factor:

$$F\left(\frac{a}{b}\right) = 1.85 - 3.38\left(\frac{a}{b}\right) + 13.24\left(\frac{a}{b}\right)^2 - 23.26\left(\frac{a}{b}\right)^3 + 16.8\left(\frac{a}{b}\right)^4 \quad (18)$$

Using the above equations and test data (Figure 12c), the fracture toughness K_{Ic} values for GaN and diamond were

calculated to be 1.75 ± 0.2 and 4.70 ± 0.6 MPa·m^{1/2}, respectively. It is worth noting that although no pre-notch was introduced for the diamond, it was assumed to have an initial flaw similar to the seeding particle diameter; indeed, our results are consistent with the literature value of 5–6 MPa·m^{1/2}.⁶⁷ In addition to the analytical solution a finite element (FE) simulation based on continuum model was run on this cantilever experiment (Appendix III in the Supporting Information) where nonlinear elastic fracture toughness J_{Ic} was derived for GaN and diamond. Equivalent K_{Ic} values were then back-calculated from the J -values assuming the mode-I J – K_I equivalence. The FE analysis gives a K_{Ic} of 3.66 ± 0.3 MPa·m^{1/2} for GaN and 5.40 ± 0.5 MPa·m^{1/2} for the diamond which are nominally consistent with the results derived from the analytical model. Appendix III also includes an example of creating microcantilevers based on the blisters; the results are comparable with the notched cantilever geometry.

To derive the toughness of the interface, the He and Hutchinson⁶⁸ analysis based fracture toughness (G_{Ic}) of the diamond can be used (Figure 13):

$$G_{Ic} = \frac{K_{Ic}^2}{E_1} \quad (19)$$

where E_1 is the Young's modulus of the diamond. The analysis, shown in Figure 13a, considers a crack in the top material (GaN) approaching the interface. The crack can arrest at or deflect along the interface, or it can penetrate the material beneath (diamond). For example, in the current experiment a single side deflection occurred at the interface (Figure 12b) which fits with the solution in Figure 13b. He and Hutchinson⁶⁸ developed their analytical solution based on the Dundurs' parameter⁶⁹ (details on Dundurs' parameters are included in Appendix I in the Supporting Information), which describes the elastic mismatch, of the system:

$$\alpha = \frac{E'_1 - E'_2}{E'_1 + E'_2} \quad (20)$$

where E'_i is the plane strain Young's modulus, given by

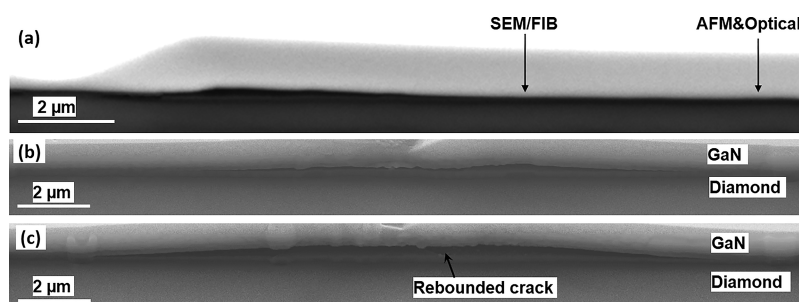


Figure 14. (a) Typical example demonstrating the difference in the crack length measured using SEM/FIB, as compared to measurements using AFM and optical microscopy. (c) Rebounded crack in (b) after further sectioning.

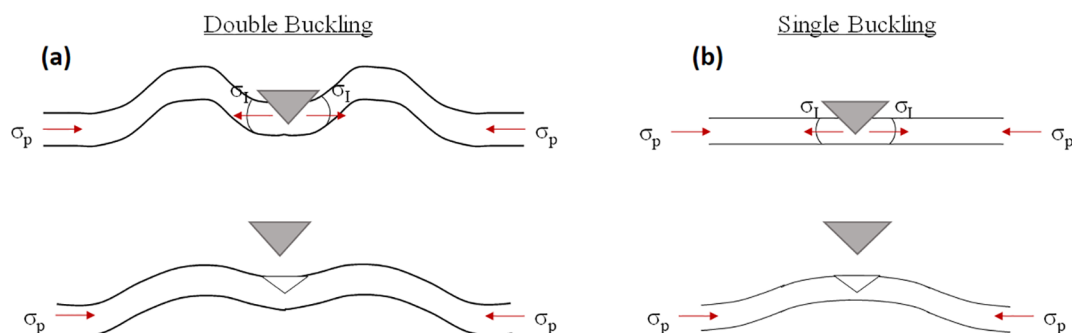


Figure 15. Different processes between (a) double pinned buckling and (b) single unpinned buckling.

$$E'_i = \frac{E_i}{(1 - \nu_i^2)} \quad (21)$$

For the present GaN-on-Diamond material, where the crack direction is from the GaN into the diamond, the first Dundurs' parameter, α , was calculated to be 0.55; if it was vice versa, $\alpha = -0.55$. When used with Figure 13c, interfacial toughness (in energy terms) needs to be more than 0.51 times that of the diamond, i.e., in terms of a stress intensity $\sim 2.5 \text{ MPa}\cdot\text{m}^{1/2}$, for the crack not to deflect at the interface.

4. DISCUSSION

4.1. Experimental Parameters for Blistering Tests.

Although FIB sectioning has been often used to measure blister dimensions in literature,^{15,63} it was found in the present work that for GaN-on-Diamond, or presumably for ceramic–ceramic interfaces with small buckle heights, FIB sectioning cannot provide reliable measurements, as shown in Figure 14. The unreliability of the radius measurements is most likely due to crack closure; removing nearly half the blister by FIB milling allows the crack to relax and close, making it hard to resolve. The buckle height can grow as it becomes less constrained by surrounding material. An extreme example of a rebounded crack is shown in Figure 14c. AFM and optical measurements, conversely, can provide good agreement for blister radii measurements (Figure 5). With optical measurements, interference techniques⁵⁷ and polarized light,⁶³ such as Nomarski contrast, can be used to increase resolution. It is therefore suggested that for GaN-on-Diamond material, AFM, when used with appropriate parameters, can provide the most reliable characterization of the geometry of buckle/blister.

4.2. Pinned or Unpinned. As can be seen from Table 3, the fracture toughness showed a significant difference depending on the choice of the constant, μ , in eq 1, i.e., an unpinned condition for a single buckle and a pinned condition assuming

a double buckle. However, the data provided by the alternative methods of two-step and microcantilever bending suggest that for GaN-on-Diamond, although there is usually a dip at the center of the indent, it is more reasonable to consider the buckles as “unpinned”. This mode must be understood fully to provide the basis for GaN-on-Diamond type of materials. Therefore, a schematic of this phenomenon is shown in Figure 15 for a film on a substrate structure.

It is emphasized here that the key difference between the two modes is that double buckles occur on loading whereas single buckles occur on unloading.^{15,16} In double buckling (pinned), the crack grows sufficiently far which reduces the buckling stress for the annulus below the indenter tip (σ_t) and edge (σ_p) stresses, i.e., σ_B falls rapidly with increasing crack length (Figure 6b); the result is that the annulus forms double buckles (Figure 15c),^{15,16,29} and the cross-section appears as two near-symmetric buckles on either side of the indenter tip.^{15,16,29} Single buckles, conversely, are caused by σ_p on unloading when the indenter tip is being removed, i.e., when the constraint on the film is removed.^{15,16,29} The whole crack acts as one large plate such that σ_B is low and $\sigma_p > \sigma_B$.^{16,29,61} However, double buckles can rebound elastically on unloading and appear unbuckled.^{16,35}

The following are the most agreed criteria for identifying double buckling:^{15,16,34,35,63} double buckles (i) have gradual surface profiles up to the indent, whereas single buckles have sharper profiles, (ii) are symmetric about the center of the indent, and (iii) have centers that are still in contact with the film. In the present work, the line profiles were all asymmetric and sharp, strongly suggesting unpinned buckling. This argument is additionally supported by the consistency in the results derived using unpinned constant, μ , and that obtained from two-step and microcantilever methods. For the FIB slices in Figure 14, the indent centers appear to have a dip at the center; however, the buckles are not symmetrical which

excludes the possibility for double buckling. It worth noting, though, that when using a Berkovich tip rather than a 90° conical indenter,^{34–36,63} there could be localized compression under the indent which may constrain the center of the indent from becoming free, but this should not be mistaken as “pinned” double buckling.

4.3. Engineering a Stronger Interface. From the three types of GaN-on-Diamond materials, a smooth interface appears to lead to an improved TBR_{eff} (see Gen 3 material in Table 1), but reduces the interfacial fracture toughness. On the other hand, introducing zigzag or undulating features to increase fracture surface area is at the cost of the thermal boundary resistance. This is consistent with a decreased phonon scattering at a smoother interface. For an ideal optimized material, a balance between the two aspects needs to be achieved.

Although the current GaN-on-Diamond system has shown improved interfacial stability compared with earlier generations of materials (Tables 3 and 4), their toughness is still lower than, for example, GaN grown on Si, where $G_{IC} > 2.96 \pm 0.4 \text{ J}\cdot\text{m}^{-2}$. It is however comparable to the toughness of interfaces where SiN_x is grown on other materials such as GaAs, where $G_{IC} = 0.76\text{--}2.59 \text{ J}\cdot\text{m}^{-2}$.^{46,48} Diamond, SiN_x and GaN are all covalently bonded; as the diamond particles are sprinkled onto the SiN_x , the SiN_x /diamond seeding particle interface is originally bonded by van der Waals forces, though during the growth process typically carbides and covalent bonds form. In addition, as the interface is incoherent, plastic and elastic discontinuities will almost certainly exist in the interface. Accordingly, we believe that improving the bonding between the SiN_x and the diamond seeds represents a key to enhancing the toughness of the GaN-on-Diamond interface.

One solution to this is to introduce scratches to the SiN_x layer and match the size of the scratches to the seeding-particle size to develop a tougher interface, similar to that in the Gen 2 material. Ohji et al.⁷⁰ showed that nanoparticles can cause bridging by deflecting the crack around them. Adding larger seeding particles could have a similar effect, as this would induce a tougher interface but without raising the effective thermal boundary resistance. The intent would be to align the larger particles with the scratches to generate crack bridging around linear clusters as seen in the Gen 2 material. To further increase the interfacial toughness, the diamond particles could be embedded into the SiN_x to create intrinsic strong bonds between the two phases together with a mechanical “keying” mechanism at the interface. To achieve this, the seeding layer could be gently “compressed” after ultrasound dispersion. Alternatively, the seeding particles could be introduced during SiN_x growth, although this may not be practical.

However, the prime objective of this study was to assist the development of GaN-on-Diamond materials by assuring the structural integrity of the GaN_x /diamond interface through an assessment of reliable surface-based approaches to evaluate their interfacial fracture toughness. Suffice to say that, by a comprehensive study combining experimental and analytical methods, the basis for the quantification of interfacial toughness in GaN-on-Diamond materials has been established and can be implemented to new designs in a very straightforward way.

5. CONCLUSIONS

A reliable surface-based nanoindentation method for the evaluation of GaN-on-Diamond system has been proposed

through systematic experimental measurements and rigorous examination of analytical methods. It is suggested that improving the attachment between the SiN_x and the diamond seeds represents a key to enhancing the toughness of the GaN-on-Diamond interface. There are two primary conclusions:

(i) Two indentation methods, that involving the development of a blistering from either a single monotonically loaded indent or a two-step indentation process, are capable of measuring consistent fracture toughness values for interfaces between GaN and diamond. The Marshall and Evans analysis of indentation-induced buckles was found to be inaccurate for GaN-on-Diamond material, most likely due to the lack of elastic indentation stress considerations.

(ii) For the GaN-on-Diamond interfaces, the mode I fracture toughness (G_{IC}) values were found to be $0.66 \pm 0.2 \text{ J}\cdot\text{m}^{-2}$ (monotonic method) and $0.57 \pm 0.2 \text{ J}\cdot\text{m}^{-2}$ (two-step method) for Gen 1 material, $0.87 \pm 0.1 \text{ J}\cdot\text{m}^{-2}$ (monotonic) and $0.91 \pm 0.3 \text{ J}\cdot\text{m}^{-2}$ (two-step) for Gen 2 material, and $0.55 \pm 0.1 \text{ J}\cdot\text{m}^{-2}$ (monotonic) and $0.53 \pm 0.2 \text{ J}\cdot\text{m}^{-2}$ (two-step) for Gen 3 material. The Gen 2 material was found to display the toughest interface, which was attributed to the scratched SiN_x matching the seeding particle size.

■ ASSOCIATED CONTENT

Supporting Information

The Supporting Information is available free of charge on the ACS Publications website at DOI: 10.1021/acsaelm.8b00091.

Phase angle and interface fracture mechanics; calculation of the parameters for the centroid and moments of inertia; linear elastic finite element simulation of microcantilever bending (PDF)

■ AUTHOR INFORMATION

Corresponding Author

*E-mail: dong.liu@bristol.ac.uk.

ORCID

Dong Liu: 0000-0002-5947-8362

Robert O. Ritchie: 0000-0002-0501-6998

Notes

The authors declare no competing financial interest.

■ ACKNOWLEDGMENTS

This work was in part supported by the UK Engineering and Physical Science Research Council (EPSRC) under the program grant GaN-DaME (EP/P00945X). D.L. acknowledges EPSRC for a Research Fellowship (EP/N004493/1) and the Royal Commission for the Exhibition of 1851 for the Brunel Research Fellowship award. Support for R.O.R. was provided by the U.S. Department of Energy, Office of Science, Office of Basic Energy Sciences, Materials Sciences and Engineering Division, under Contract No. DE-AC02-05CH11231. The authors acknowledge Prof. James Marrow (Univ. Oxford) for useful discussions and Prof. David Armstrong (Univ. Oxford) for the use of the nanoindenter.

■ REFERENCES

- (1) Sun, H.; Simon, R. B.; Pomeroy, J. W.; Francis, D.; Faili, F.; Twitchen, D. J.; Kuball, M. Reducing GaN-on-diamond interfacial thermal resistance for high power transistor applications. *Appl. Phys. Lett.* **2015**, *106*, 111906.
- (2) Manoi, A.; Pomeroy, J. W.; Killat, N.; Kuball, M. Benchmarking of thermal boundary resistance in AlGaIn/GaN HEMTs on SiC

substrates: Implications of the nucleation layer microstructure. *IEEE Electron Device Lett.* **2010**, *31*, 1395–1397.

(3) Pomeroy, J. W.; Bernardoni, M.; Dumka, D. C.; Fanning, D. M.; Kuball, M. Low thermal resistance GaN-on-diamond transistors characterized by three-dimensional Raman thermography mapping. *Appl. Phys. Lett.* **2014**, *104*, 083513.

(4) Jessen, G. H.; Gillespie, J. K.; Via, G. D.; Crespo, A.; Langley, D.; Wasserbauer, J.; Faili, F.; Francis, D.; Babic, D.; Ejeckam, F.; Guo, S.; Eliashevich, I. AlGaIn/GaN HEMT on diamond technology demonstration. *Technol. Dig. - IEEE Compd. Semicond. Integr. Circuit Symp. CSIC 2006*, 271–274.

(5) Dumka, D. C.; Saunier, P. AlGaIn/GaN HEMTs on diamond substrate. *65th DRC Device Res. Conf.* **2007**, *25*, 31–32.

(6) Tyhach, M.; Altman, D.; Bernstein, S.; Korenstein, R.; Cho, J.; Goodson, K. E.; Francis, D.; Faili, F.; Ejeckam, F.; Kim, S.; Graham, S. Next generation gallium nitride HEMTs enabled by diamond substrates. *Lester Eastman Conf. High Perform. Devices 2014*, S2-T3.

(7) Ejeckam, F.; Francis, F.; Firooz, F.; Twitchen, D.; Bolliger, B.; Babic, D.; Felbinger, J. GaN-on-diamond: A brief history. *Lester Eastman Conf. High Perform. Devices 2014*, 1–5.

(8) Chao, P.-C.; Chu, K.; Creamer, C.; Diaz, J.; Yurovchak, T.; Shur, M.; Kallaher, R.; McGray, C.; Via, G. D.; Blevins, J. D. Low-Temperature Bonded GaN-on-Diamond HEMTs With 11 W/mm Output Power at 10 GHz. *IEEE Trans. Electron Devices* **2015**, *62*, 3658–3664.

(9) Van Dreumel, G. W. G.; Tinnemans, P. T.; Van Den Heuvel, A. A. J.; Bohnen, T.; Buijsters, J. G.; Ter Meulen, J. J.; Van Enckevort, W. J. P.; Hageman, P. R.; Vlieg, E. Realising epitaxial growth of GaN on (001) diamond. *J. Appl. Phys.* **2011**, *110*, 013503.

(10) Hirama, K.; Kasu, M.; Taniyasu, Y. RF high-power operation of AlGaIn/GaN HEMTs epitaxially grown on diamond. *IEEE Electron Device Lett.* **2012**, *33*, 513–515.

(11) Alomari, M.; Dussaigne, A.; Martin, D.; Grandjean, N.; Gaquiere, C.; Kohn, E. AlGaIn/GaN HEMT on (111) single crystalline diamond. *Electron. Lett.* **2010**, *46*, 299.

(12) Cho, J.; Francis, D.; Altman, D. H.; Asheghi, M.; Goodson, K. E. Phonon conduction in GaN-diamond composite substrates. *J. Appl. Phys.* **2017**, *121*, 055105.

(13) Francis, D.; Faili, F.; Babi, D.; Ejeckam, F.; Nurmikko, A.; Maris, H. Formation and characterization of 4-in. GaN-on-diamond substrates. *Diamond Relat. Mater.* **2010**, *19*, 229–233.

(14) Dumka, D. C.; Francis, D.; Chou, T. M.; Ejeckam, F.; Faili, F. AlGaIn/GaN HEMTs on diamond substrate with over 7 W/mm output power density at 10 GHz. *Electron. Lett.* **2013**, *49*, 1298–1299.

(15) Gerberich, W. W.; Cordill, M. J. Physics of adhesion. *Rep. Prog. Phys.* **2006**, *69*, 2157–2203.

(16) Volinsky, A.; Moody, N.; Gerberich, W. Interfacial toughness measurements for thin films on substrates. *Acta Mater.* **2002**, *50*, 441–466.

(17) Wang, X.; Wang, C.; Atkinson, A. Interface fracture toughness in thermal barrier coatings by cross-sectional indentation. *Acta Mater.* **2012**, *60*, 6152–6163.

(18) Zhao, P. F.; Sun, C. A.; Zhu, X. Y.; Shang, F. L.; Li, C. J. Fracture toughness measurements of plasma-sprayed thermal barrier coatings using a modified four-point bending method. *Surf. Coat. Technol.* **2010**, *204*, 4066–4074.

(19) Hofinger, I.; Oechsner, M.; Bahr, H.; Swain, M. V. Modified four-point bending specimen for determining the interface fracture energy for thin, brittle layers. *Int. J. Fract.* **1998**, *92*, 213–220.

(20) Eberl, C.; Wang, X.; Gianola, D. S.; Nguyen, T. D.; He, M. Y.; Evans, A. G.; Hemker, K. J. In situ measurement of the toughness of the interface between a thermal barrier coating and a Ni alloy. *J. Am. Ceram. Soc.* **2011**, *94*, 120–127.

(21) Dauskardt, R. H.; Lane, M.; Ma, Q.; Krishna, N. Adhesion and debonding of multi-layer thin film structures. *Eng. Fract. Mech.* **1998**, *61*, 141–162.

(22) Volinsky, A. A.; Vella, J. B.; Gerberich, W. W. Fracture toughness, adhesion and mechanical properties of low-K dielectric

thin films measured by nanoindentation. *Thin Solid Films* **2003**, *429*, 201–210.

(23) Charalambides, P. G.; Lund, J.; Evans, A. G.; McMeeking, R. M. A test specimen for determining the fracture resistance of bimaterial interfaces. *J. Appl. Mech.* **1989**, *56*, 77.

(24) Charalambides, P. G.; Cao, H. C.; Lund, J.; Evans, A. G. Development of a test method for measuring the mixed mode fracture resistance of bimaterial interfaces. *Mech. Mater.* **1990**, *8*, 269–283.

(25) Atkinson, C.; Smelser, R. E.; Sanchez, J. Combined mode fracture via the cracked Brazilian disk test. *Int. J. Fract.* **1980**, *18*, 279–291.

(26) Wang, J. S.; Suo, Z. Experimental determination of interfacial toughness curves using Brazil-nut-sandwiches. *Acta Metall. Mater.* **1990**, *38*, 1279–1290.

(27) Ma, Q. A four-point bending technique for studying subcritical crack growth in thin films and at interfaces. *J. Mater. Res.* **1997**, *12*, 840–845.

(28) Dannenberg, H. Measurement of adhesion by a blister method. *J. Appl. Polym. Sci.* **1961**, 125–134.

(29) Chen, J.; Bull, S. J. Approaches to investigate delamination and interfacial toughness in coated systems: an overview. *J. Phys. D: Appl. Phys.* **2011**, *44*, 034001.

(30) Bagchi, A.; Lucas, G. E.; Suo, Z.; Evans, A. G. A new procedure for measuring the decohesion energy for thin ductile films on substrates. *J. Mater. Res.* **1994**, 1734–1741.

(31) Marshall, D. B.; Evans, A. G. Measurement of adherence of residually stressed thin films by indentation. I. Mechanics of interface delamination. *J. Appl. Phys.* **1984**, *56*, 2632–2638.

(32) Kriese, M. D.; Gerberich, W. W.; Moody, N. R. Quantitative adhesion measures of multilayer films: Part I. Indentation Mechanics. *J. Mater. Res.* **1999**, *14*, 3007.

(33) Cordill, M. J.; Bahr, D. F.; Moody, N. R.; Gerberich, W. W. Adhesion measurements using telephone cord buckles. *Mater. Sci. Eng., A* **2007**, *443*, 150–155.

(34) Kleinbichler, A.; Pfeifenberger, M. J.; Zechner, J.; Moody, N. R.; Bahr, D. F.; Cordill, M. J. New insights into nanoindentation-based adhesion testing. *JOM* **2017**, *69* (11), 2237–2245.

(35) Kleinbichler, A.; Zechner, J.; Cordill, M. J. Buckle induced delamination techniques to measure the adhesion of metal dielectric interfaces. *Microelectron. Eng.* **2017**, *167*, 63–68.

(36) Waters, P.; Volinsky, A. A. Stress and moisture effects on thin film buckling delamination. *Exp. Mech.* **2007**, *47*, 163–170.

(37) Volinsky, A.; Moody, N. R.; Gerberich, W. W. Superlayer residual stress effect on the indentation adhesion measurements. *MRS Online Proc. Libr.* **1999**, 383 DOI: 10.1557/PROC-594-383.

(38) Kuzel, R.; Valvoda, V.; Chladek, M.; Musil, J.; Matous, J. XRD microstructural study of Zn films deposited by unbalanced magnetron sputtering. *Thin Solid Films* **1995**, *263*, 150–158.

(39) Musil, J.; Baroch, P.; Vlček, J.; Nam, K. H.; Han, J. G. Reactive magnetron sputtering of thin films: present status and trends. *Thin Solid Films* **2005**, *475*, 208–218.

(40) Chang, J.; Shen, C.; Hon, M. Growth characteristics and residual stress of RF magnetron sputtered ZnO:Al films. *Ceram. Int.* **2003**, *29*, 245–250.

(41) Kelly, P. J.; Arnell, R. D. Magnetron sputtering: a review of recent developments and applications. *Vacuum* **2000**, *56*, 159–172.

(42) Sanchez, J.; El-Mansy, S.; Sun, B.; Scherban, T.; Fang, N.; Pantoso, D.; Ford, W.; Elizalde, M.; Martinez-Esnaola, J.; Martin-Meizoso, A.; Gil-Sevillano, J.; Fuentes, M.; Maiz, J. Cross-sectional nanoindentation: a new technique to measure thin film interfacial adhesion. *Acta Mater.* **1999**, *47*, 4405.

(43) De Boer, M. P.; Gerberich, W. W. Microwedge indentation of the thin film line-I. Mechanics. *Acta Mater.* **1996**, *44*, 3169.

(44) De Boer, M. P.; Gerberich, W. W. Microwedge indentation of the thin film fine line - II. Experiment. *Acta Mater.* **1996**, *44*, 3177–3187.

- (45) Hainsworth, S.; McGurk, M.; Page, T. The effect of coating cracking on the indentation response of thin hard-coated systems. *Surf. Coat. Technol.* **1998**, *102*, 97–107.
- (46) Xie, H.; Huang, H. Characterization of the interfacial strength of SiNx/GaAs film/substrate systems using energy balance in nanoindentation. *J. Mater. Res.* **2013**, *28*, 3137–3145.
- (47) Lu, M.; Huang, H. Interfacial energy release rates of SiN/GaAs film/substrate systems determined using a cyclic loading dual-indentation method. *Thin Solid Films* **2015**, *589*, 822–830.
- (48) Lu, M.; Huang, H. Determination of the energy release rate in the interfacial delamination of silicon nitride film on gallium arsenide substrate via nanoindentation. *J. Mater. Res.* **2014**, *29*, 801–810.
- (49) Wei, P. J.; Liang, W. L.; Ai, C. F.; Lin, J. F. A new method for determining the strain energy release rate of an interface via force-depth data of nanoindentation tests. *Nanotechnology* **2009**, *20*, 025701.
- (50) Zhou, Y.; Ramaneti, R.; Anaya, J.; Korneychuk, S.; Derluyn, J.; Sun, H.; Pomeroy, J.; Verbeeck, J.; Haenen, K.; Kuball, M. Thermal characterization of polycrystalline diamond thin film heat spreaders grown on GaN HEMTs. *Appl. Phys. Lett.* **2017**, *111*, 041901.
- (51) Williams, O. A.; Nesladek, M.; Daenen, M.; Michaelson, S.; Hoffman, A.; Osawa, E.; Haenen, K.; Jackman, R. B. Growth, electronic properties and applications of nanodiamond. *Diamond Relat. Mater.* **2008**, *17*, 1080–1088.
- (52) Twitchen, D. J.; Sun, H.; Liu, D.; Pomeroy, J. W.; Francis, D.; Faili, F.; Twitchen, D. J.; Kuball, M. GaN-on-diamond: Robust mechanical and thermal properties. In *2016 International Conference on Compound Semiconductor Manufacturing Technology*, Miami, Florida, May 16–19, 2016; pp 201–204.
- (53) Oliver, W. C.; Pharr, G. M. An improved technique for determining hardness and elastic modulus using load and displacement sensing indentation experiments. *J. Mater. Res.* **1992**, *7*, 1564–1583.
- (54) Tsai, C. H.; Jian, S. R.; Juang, J. Y. Berkovich nanoindentation and deformation mechanisms in GaN thin films. *Appl. Surf. Sci.* **2008**, *254*, 1997–2002.
- (55) Nowak, R.; Pessa, M.; Suganuma, M.; Leszczynski, M.; Grzegory, I.; Porowski, S.; Yoshida, F. Elastic and plastic properties of GaN determined by nano-indentation of bulk crystal. *Appl. Phys. Lett.* **1999**, *75*, 2070.
- (56) Nečas, D.; Klapetek, P. Gwyddion: An open-source software for SPM data analysis. *Cent. Eur. J. Phys.* **2012**, *10*, 181–188.
- (57) Rossington, C.; Evans, A. G.; Marshall, D. B.; Khuri-Yakub, B. T. Measurements of adherence of residually stressed thin films by indentation. II. Experiments with ZnO/Si. *J. Appl. Phys.* **1984**, *56*, 2639–2644.
- (58) Lawn, B. R.; Evans, A.; Marshall, D. B. Elastic/Plastic indentation damage in ceramics: The lateral crack system. *J. Am. Ceram. Soc.* **1980**, *63*, 574–581.
- (59) Chen, X.; Hutchinson, J. W.; Evans, A. G. The mechanics of indentation induced lateral cracking. *J. Am. Ceram. Soc.* **2005**, *88*, 1233–1238.
- (60) Evans, A. G.; Hutchinson, J. W. On the mechanics of delamination and spalling in compressed films. *Int. J. Solids Struct.* **1984**, *20*, 455–466.
- (61) Hutchinson, J. W.; Suo, Z. Mixed mode cracking in layered materials. *Adv. Appl. Mech.* **1991**, *29*, 63–191.
- (62) Caldas, P. G.; Silva, E. M.; Prioli, R.; Huang, J. Y.; Juday, R.; Fischer, A. M.; Ponce, F. A. Plasticity and optical properties of GaN under highly localized nanoindentation stress fields. *J. Appl. Phys.* **2017**, *121*, 125105.
- (63) Cordill, M. J.; Bahr, D. F.; Moody, N. R.; Gerberich, W. W. Recent developments in thin film adhesion measurement. *IEEE Trans. Device Mater. Reliab.* **2004**, *4*, 163–168.
- (64) Swanson, P. L.; Fairbanks, C. J.; Lawn, B. R.; Mai, Y.-W.; Hockey, B. J. Crack interface grain bridging as a fracture resistance I, Mechanism in ceramics: I, Experimental study on alumina. *J. Am. Ceram. Soc.* **1987**, *70*, 279–289.
- (65) Miyazato, T.; Hojo, M.; Sugano, M.; Adachi, T.; Inoue, Y.; Shikimachi, K.; Hirano, N.; Nagaya, S. Mode I type delamination fracture toughness of YBCO coated conductor with additional Cu layer. *Phys. C* **2011**, *471*, 1071–1074.
- (66) Di Maio, D.; Roberts, S. G. Measuring fracture toughness of coatings using focused-ion-beam-machined microbeams. *J. Mater. Res.* **2005**, *20*, 299–302.
- (67) Drory, M. D.; Dauskardt, R. H.; Kant, A.; Ritchie, R. O. Fracture of synthetic diamond. *J. Appl. Phys.* **1995**, *78*, 3083–3088.
- (68) Ming-Yuan, H.; Hutchinson, J. W. Crack Deflection at an interface between dissimilar elastic materials. *Int. J. Solids Struct.* **1989**, *25*, 1053–1067.
- (69) Dundurs, J. Discussion: Edge-bonded dissimilar orthogonal elastic wedges under normal and shear loading. *J. Appl. Mech.* **1969**, *36*, 650–652.
- (70) Ohji, T.; Jeong, Y.-K.; Choa, Y.-H.; Niihara, K. Strengthening and Toughening Mechanisms of Ceramic Nanocomposites. *J. Am. Ceram. Soc.* **1998**, *81*, 1453–1460.